Fundamental Research 6 (2026) 1985–1997

Contents lists available at ScienceDirect

Fundamental Research

journal homepage: http://www.keaipublishing.com/en/journals/fundamental-research/

Article

Spatial atlas of human diabetic kidney uncovered podocyte-driven metabolic-inflammatory crosstalk via glycerolipid reprogramming and DUSP4/MMP3 axis ☆

Shi Qiu [a], Zhibo Wang [a], Sifan Guo [a], Dandan Xie [a], Ying Cai [a], Xian Wang [a], Qiang Yang [b], Qiqi Zhao [b], Yu Guan [b], Chunsheng Lin [b], Hong Yao [c], Songqi Tang [a,*], Wenjie Sun [d,*], Yiqiang Xie [a,*], Aihua Zhang [a,b,*]

[a] School of Chinese Medicine, International Advanced Functional Omics Platform, Scientific Experiment Center, Hainan Medical University, Haikou 571199, China
[b] College of Basic Medicine, Graduate School, Second Affiliated Hospital, Heilongjiang University of Chinese Medicine, Harbin 150040, China
[c] First Affiliated Hospital, Harbin Medical University, Harbin 150040, China
[d] Department of Nephrology, Traditional Chinese Medicine Integrated Department of Nephrology, The First Affiliated Hospital of Zhengzhou University, Zhengzhou 450052, China

ARTICLE INFO

Article history:
Received 8 September 2025
Received in revised form 30 January 2026
Accepted 13 February 2026
Available online 20 February 2026

Keywords:
Spatial transcriptomics
Podocytes
DUSP4-MAPK pathway
Glycerolipid metabolism
MMP3

ABSTRACT

Diabetic nephropathy (DN) pathogenesis remains elusive due to the lack of comprehensive spatial molecular characterization related to tissue pathological signatures. Here, we construct the spatial single-cell atlas of human DN kidneys using clinical formalin-fixed paraffin-embedded (FFPE) biopsies, integrating spatial transcriptomics, metabolomics, and scRNA-seq across 39,006 cells. We identify podocytes as spatial metabolic-inflammatory hubs orchestrating DN progression, exhibiting conserved dysregulation of glycerolipid metabolism and MAPK signaling in human and diabetic mice kidneys. Spatial multi-omics of inflammatory and glomerular injury zones reveal 179 and 234 differentially expressed genes enriched in MAPK pathways. Crucially, urinary MMP3, traced to glomerular injury zones, emerges as a non-invasive diagnostic biomarker. We further demonstrate that astragaloside IV (ASIV) attenuates DN by dual targeting: rescuing DUSP4-mediated MAPK suppression (reducing p-p38/JNK) and normalizing glycerolipid metabolites (D-glycerate, 3-PGA), thereby downregulating MMP3/IL-6/IL-1β and suppressing oxidative stress in podocytes. This work redefines DN as a disorder of spatially organized metabolic-inflammation synergy, establishing urinary MMP3 for clinical detection and ASIV as a therapeutic agent targeting the DUSP4-MAPK-glycerolipid axis, providing a roadmap for precision interventions in DN.

1. Introduction

Diabetic nephropathy (DN), the primary driver of end-stage renal disease, affects 30%–40% of diabetics worldwide, yet its spatial pathophysiology remains unresolved [1,2]. Conventional molecular profiling disrupts cellular microenvironments, masking region-specific mechanisms underlying glomerulosclerosis, interstitial fibrosis, and inflammatory cascades [3–6]. A critical knowledge gap persists: how spatially organized metabolic-inflammatory crosstalk drives regional glomerulotubular injury [7]. While single-cell atlases reveal transcriptional heterogeneity in chronic kidney disease, they lack spatial context-a major limitation given the kidney's intricate corticomedullary zonation and specialized niches [8,9]. Spatial transcriptomics could bridge this gap, but its application to DN has been hindered by technical challenges, especially with formalin-fixed paraffin-embedded (FFPE) biopsies [10]. Resolving these spatial changes is essential to uncover the therapeutic targets and DN progression [11].

Spatial multi-omics technologies now enable mapping of molecular heterogeneity while preserving tissue architecture-a breakthrough for organs like the kidney [12–14]. DN progression hinges on cell crosstalk among glomerular, tubular, and immune cells within tissue microenvironments, yet the spatial orchestration of metabolic dysregulation and immune infiltration remains poorly defined [15]. Single-cell studies fail to localize injury-specific signaling axes, and the key therapeutic pathways remain undiscovered [16]. To address this, we present a spatial transcriptomics atlas of diabetic mouse and human kidneys, integrating multi-omics with histopathology. Our approach combines spatially resolved transcriptomics of FFPE biopsies and metabolic imaging (MALDI-MS) to link dysregulated pathways with injury regions.

☆ Peer review under the responsibility of Editorial Board of Fundamental Research.

* Corresponding authors.
E-mail addresses: tangsongqi@hainmc.edu.cn (S. Tang), wsun@une.edu (W. Sun), xieyiqiang@hainmc.edu.cn (Y. Xie), aihuatcm@163.com (A. Zhang).

https://doi.org/10.1016/j.fmre.2026.02.005

To directly link cellular pathophysiology with tissue microarchitecture, we established an integrated multi-omics platform compatible with clinical FFPE renal biopsies. Our primary objective was to delineate the compartment-specific metabolic-inflammatory crosstalk driving regional injury, particularly within glomerular and inflammatory niches. We further validated mechanistic insights and therapeutic targets using a diabetic mouse model and in vitro podocyte assays. Through this strategy, we sought to identify spatially organized disease drivers, discover clinically actionable biomarkers, and elucidate novel therapeutic axes for DN.

2. Experimental methods

2.1. Human subjects

This study was conducted in full accordance with the ethical guidelines outlined in the Declaration of Helsinki. The Institutional Review Board of the First Affiliated Hospital of Hainan Medical University reviewed and approved all protocols involving human participants (Approval No. ChiCTR2400087438). The study cohort comprised 23 individuals diagnosed with diabetic nephropathy (DN) and 20 age- and sex-matched healthy control (HC) volunteers. Clinical samples collected included urine (targeted for metabolomic and proteomic analysis) from 20 participants and FFPE renal tissue sections (for spatial transcriptomic profiling) from 3 patients. Kidney tissue sections were processed sequentially for spatial transcriptomic and histopathological evaluation. Urine samples from control participants underwent the same comprehensive metabolic and proteomic analyses.

Detailed demographic and clinical parameters for all 43 participants (23 DN, 20 HC) are provided in Supplementary Table S1. Statistical comparison confirmed no significant differences between groups regarding age, sex, body weight, or body mass index (BMI). In contrast, the DN group demonstrated significant impairment in renal function and metabolic homeostasis, characterized by substantially elevated levels of serum creatinine, blood urea nitrogen (BUN), uric acid, and fasting blood glucose, accompanied by a markedly reduced estimated glomerular filtration rate (eGFR) relative to the healthy controls (all $p < 0.05$).

2.2. Histopathological examination of human renal FFPE specimens

Renal tissues were fixed in 4% paraformaldehyde and processed following standard histopathological procedures. Specimens were examined using a Nikon Eclipse Ci-L microscope and digitized with a 3DHISTECH PANNORAMIC scanner. High-resolution digital images were captured using SlideViewer2.5 software. Pathological evaluation included systematic scoring of tubular atrophy, interstitial fibrosis, inflammatory cell infiltration, and glomerular changes. Critical morphological alterations were marked with color-coded arrows for accurate spatial reference. Both manual microscopic review and whole-slide digital scanning ensured thorough assessment across cortical and medullary compartments.

2.3. Spatial transcriptomic profiling via Visium HD

Renal biopsy specimens were processed for high-definition spatial transcriptomics using an optimized FFPE workflow. Freshly obtained kidney puncture tissues were cleared of debris, dissected into 6.5 mm^2 segments, and promptly fixed in 4% paraformaldehyde prior to paraffin embedding. Sections of 5 μm thickness were placed on adhesive slides (Sigma-Aldrich, P0425). Deparaffinization, hematoxylin-eosin staining, and antigen retrieval were performed according to the 10x Genomics FFPE protocol (CG000684). Visium HD spatial profiling was carried out on 6.5 mm^2 slides (10x Genomics, PN-2000970) using the Human Spatial Gene Expression Reagent Kit (PN-1000675). Probe hybridization, tissue transfer via CytAssist, and library preparation followed the manufacturer's instructions (CG000085). Final libraries were sequenced in a paired-end 150-bp configuration on an Illumina platform.

2.4. Specimen processing and sequencing

Renal tissue punches were subjected to spatial transcriptomic analysis using the 10x Visium HD platform. Samples were FFPE, sectioned, and mounted on standard slides. After deparaffinization, sections were stained with hematoxylin and eosin (H&E) and imaged for morphological reference. Overnight hybridization of RNA-templated ligation probes was followed by probe ligation and tissue removal to release bound probes. These probes were then captured on Visium HD slides, and subsequent cDNA synthesis, amplification, and library construction were conducted. Final libraries were sequenced via next-generation sequencing on an Illumina platform.

2.5. Dimensionality reduction and clustering of spatial transcriptome

Raw data underwent Space Ranger (v3.1.2) alignment and quality control. Spatial barcodes/UMIs assigned reads to 2 μm × 2 μm tiles, aggregated into 16 μm × 16 μm analytical units. The empty bins were removed during quality control. Key quality metrics from Space Ranger quantification are provided in the report: the number of high-quality bins per sample ranged from 8700 to 20,213; the average UMI counts per bin varied between 443 and 2646; and the average number of genes detected per bin spanned from 359 to 1769. Sequencing saturation, a critical quality indicator, reached 88.4% in representative samples. Following quantification, gene expression data were normalized using the global-scaling log-normalize method. Due to noticeable batch effects across samples, Harmony was employed for batch correction prior to dimensionality reduction. Uniform Manifold Approximation and Projection (UMAP) was applied for visualization and clustering, ultimately identifying the distinct spatial clusters.

2.6. Spatial visualization and marker gene identification

Marker genes for each cluster were identified using the presto algorithm, with thresholds set at log fold change > 0 and minimum expression fraction > 0.25. Spatial distributions were mapped via heatmaps, UMAP projections, and expression maps to resolve regional patterns. Presto-based differential analysis identified inter-group differentially expressed genes (DEGs) (fold change > 1.0 and adjusted p-value < 0.05). All workflows leveraged R/Python ecosystems (Seurat v5.1.0, spacexr v2.2.0, Harmony v1.0; ggplot2) with GRCh38 references. Cell types were annotated using canonical markers (Table S2). This study employed ROC analysis to identify cell types as the key pathological contributors, followed by internal validation through cross-species consistency, spatial mapping, and pathway enrichment.

2.7. Urinary proteomic profiling in DN patients

Urinary proteins were isolated and quantified by BCA assay, then reduced with 5 mm DTT (37 °C, 1 h) and alkylated with 10 mm iodoacetamide (room temperature, 45 min, dark). After dilution with 25 mm ammonium bicarbonate, proteins were digested with trypsin (1:50 enzyme-to-substrate ratio, 37 °C, overnight) and acidified to pH < 3 to quench the reaction. Peptides were desalted on C18 cartridges, eluted with 70% acetonitrile, and lyophilized. For LC-MS/MS, samples were reconstituted in 0.1% formic acid and separated on a RIGOL L-3000 HPLC system using a 65-min gradient of 6%–95% acetonitrile/0.1% formic acid. Mass spectrometry was performed on an Orbitrap Eclipse equipped with FAIMS Pro^{TM} (compensation voltages: -45 to -65 V) in positive-ion data-dependent acquisition mode (scan range m/z 350–1500, resolution 120,000). MS/MS fragmentation was carried out at 33% collision energy with a resolution of 15,000. Raw files were processed using Proteome Discoverer 2.4 and searched against the UniProt *Homo sapiens*

database with tryptic specificity, static carbamidomethylation, dynamic oxidation, and N-terminal acetylation. Protein identifications were filtered at 1% false-discovery rate.

2.8. Metabolic analysis of urine samples in DN patients

Samples underwent 4 ˚C thawing, vortexing, and extraction in 80% methanol with 2-chloro-L-phenylalanine (4 ppm internal standard). After centrifugation (12,000 rpm, 4 ˚C, 10 min), supernatants were PTFE-filtered (0.22 μm). Metabolite separation employed a Vanquish UHPLC system with an HSS T3 column (2.1 × 100 mm, 1.8 μm) under acetonitrile/formic acid (ESI+) or acetonitrile/ammonium formate (ESI−) gradients (8%–98%). Full-scan MS/ddMS^2 analysis used an Orbitrap Exploris 120 (MS1: 60K resolution; MS2: 15K resolution; *m/z* 100–1000). Raw data conversion preceded XCMS-based peak alignment and QC filtering (RSD < 30%). Metabolite identification leveraged HMDB, KEGG, and in-house spectral libraries.

2.9. In vivo studies

All experimental protocols were conducted in compliance with institutional animal care standards and were approved by the Animal Ethics Committee of Hainan Medical University (Protocol HYLL-2023-457). Male C57BL/KsJ mice aged 7 weeks (Jiangsu Jicui Yaokang Biotechnology, License SCXK-2023-0009) of both db/m (non-diabetic) and db/db (diabetic) strains were used. Animals were randomly allocated to three groups ($n = 6$ per group): db/m receiving saline (control), db/db receiving saline, and db/db receiving ASIV (1 g/kg/day) [17,18]. Compounds were administered once daily by oral gavage for 4 weeks. Following anesthesia, kidneys were embedded in carboxymethyl cellulose, snap-frozen in liquid nitrogen, and stored at −80 ˚C.

2.10. Histopathological analysis

Kidney tissue samples were fixed, processed, and sectioned following standardized histopathological protocols. Digital whole-slide scanning was performed using a 3DHISTECH PANNORAMIC scanner, and images were analyzed with CaseViewer2.4 software. Histopathological evaluation included systematic assessment of hemorrhage, degeneration, fibrosis, and inflammatory infiltration at multiple magnifications. Key lesions were annotated using color-coded arrows for precise morphological identification.

2.11. Spatial transcriptomics analysis of mice kidney

Fresh mouse kidney tissues were processed through 4% FPA fixation and paraffin embedding. Target regions underwent sectioning and slide mounting per 10x Genomics Protocol. Subsequent deparaffinization, H&E staining, and decrosslinking followed a standardized workflow. FFPE-compatible libraries were generated with the Visium CytAssist Spatial Gene Expression kit (Mouse, PN-1000521) via manufacturer protocol, encompassing probe hybridization, CytAssist transfer, and library construction. Illumina sequencing data underwent Space Ranger processing for alignment, gene quantification, and spatial barcode assignment. Downstream analytics resolved region-specific molecular signatures through clustering, differential expression, and spatial transcriptomic mapping.

2.12. Dimensionality reduction and clustering of spatial transcriptomics

Diabetic murine kidney tissues were profiled using the 10x Genomics Visium CytAssist platform. Raw sequencing data underwent Space Ranger (v2.0.1) processing for demultiplexing, mm10 genome alignment, and gene expression matrix generation. QC metrics encompassed high-quality spot counts, mean reads/spot, median genes/spot, and sequencing saturation per sample. Technical variability was mitigated via *sctransform* normalization in Seurat (v4.3.0), preserving biological heterogeneity. The expression matrix underwent Harmony-based dimensionality reduction for batch correction, followed by UMAP visualization. Louvain clustering resolved the distinct tissue domains, with cluster stability validated for robust biological interpretation.

2.13. Spatial distribution of marker and cell type annotation

Marker genes for each cluster were identified using the presto method. Cell types were annotated using the reference single-cell RNA-seq dataset. Spatial distribution of cell types was visualized using pie charts and heatmaps to highlight compositional differences across tissue regions. Differential gene expression analysis was conducted between experimental groups (diabetic vs. control) using Seurat's FindMarkers function, with significance thresholds of p-value < 0.05 and fold change > 1.0. Spatial gene expression patterns were visualized using UMAP plots, heatmaps, and violin plots. Statistical analyses, including spot co-localization and cell type proportion comparisons, were conducted to explore spatial heterogeneity. All analyses were performed in R (v4.0.3), with visualization aided by Circlize (v0.4.10) and ggplot2.

2.14. MALDI-MSI imaging of mice kidney tissue

Murine kidney tissues underwent 4% FPA fixation and paraffin embedding. Sections (10 μm) mounted on conductive slides were subjected to MALDI-MSI (Bruker timsTOF flex) with 9-AA matrix deposition via HTX TM sprayer (90 ˚C, 10 psi, 0.12 mL/min). Negative ion mode imaging (30 μm resolution; *m/z* 150–1200; 400 shots/pixel) was acquired. Data preprocessing included baseline correction, peak alignment (10 ppm tolerance), and normalization. Metabolites were identified using HMDB/LipidMaps/KEGG with isotopic validation. The metabolic alterations were assessed via *Z*-score analysis with co-localization.

2.15. Western blot analysis

Kidney tissues underwent RIPA-based homogenization (protease/phosphatase inhibitors, 100:1), centrifugation (12,000 rpm, 25 min, 4 ˚C), and supernatant cryopreservation (−80 ˚C). Protein quantification used BCA assays ($\lambda = 562$ nm). Aliquots (30 μg) were denatured (Laemmli buffer, 100 ˚C, 10 min), electrophoresed (12.5% SDS-PAGE, 120 V, 90 min), and wet-transferred to PVDF membranes (0.45 μm). Post-blocking (1X buffer, 60 min), membranes received primary antibodies (MMP-3/IL-6/DUSP4/p-p38/p38/p-JNK/JNK/p-ERK/ERK; 1:500–1:1000, 4 ˚C/overnight) and HRP-secondaries (1:50,000, 60 min). Signals were developed via ECL (Tanon-ABL X5), with α-Tubulin/β-actin (1:10,000) as loading controls. Stripping buffer (20 min) enabled reprobing. All steps incorporated triplicate TBST washes. Band intensities were ImageJ-quantified (loading control-normalized).

2.16. Cellular studies and interventions

Mouse podocyte (MPC-5) cells were cultured in DMEM supplemented with 10% FBS and 1% penicillin-streptomycin under standard conditions (37 ˚C, 5% CO_2). At 70%–80% confluency, cells were exposed to 24-h serum-free treatments: normal glucose (CON), high glucose (MOD, 60 mm) [19,20], high glucose with 100 μm metformin (MET), and high glucose with 30 μm ASIV. After treatment, cells were rinsed with PBS, lysed in TRIzol reagent, snap-frozen in liquid nitrogen, and stored for subsequent RNA sequencing. Cell viability and morphology were regularly assessed using an inverted microscope. Six biological replicates per condition were included to ensure statistical reliability. Transcriptomic profiling was employed to delineate high-glucose-induced injury mechanisms and the protective effects of the tested compounds.

2.17. Intracellular metabolite profiling for glycerolipid metabolism

MPC-5 cell metabolites were extracted using a 2:2:1 (v/v/v) mixture of acetonitrile, methanol, and water containing 2-chloro-L-phenylalanine (4 ppm, internal standard). Homogenization was performed by bead-beating (60 Hz, 2 min), followed by centrifugation (12,000 rpm, 10 min, 4 °C). Supernatants were dried, reconstituted in 0.1% formic acid/acetonitrile (1:9), and filtered through a 0.22 μm PTFE membrane. Separation was achieved on a UPLC HSS T3 column (2.1 × 100 mm, 1.8 μm) with a 0.3 mL/min gradient using 0.1% formic acid (positive mode) or 5 mm ammonium formate (negative mode). Data were acquired on an Orbitrap Exploris 120 mass spectrometer in full-scan/ddMS^2 mode (m/z 100–1000). Raw data were processed with XCMS, normalized, and filtered (RSD < 30%). Metabolite annotation was performed against HMDB, KEGG, and LipidMaps databases prior to comparative analysis.

2.18. mRNA sequencing

MPC-5 podocyte RNA underwent TRIzol extraction, with integrity confirmed (NanoDrop 2100/Bioanalyzer). Libraries prepared via VAHTS Universal V6 Kit underwent Illumina NovaSeq 6000 sequencing. Raw reads were quality-filtered, aligned to GRCh38, and quantified. DESeq2 identified DEGs ($|\log_2 FC| > 1$; $p < 0.05$), visualized through hierarchical clustering. Functional enrichment interrogated GO/KEGG terms (hypergeometric tests) and GSEA.

2.19. Immunohistochemistry

For ROS detection, MPC-5 cells were incubated with DCFH-DA (10 μm) for 20 min, followed by DAPI nuclear staining, and imaged using a confocal microscope (FV3000, Olympus). For cytokine analysis, cells were fixed, permeabilized, and stained with anti-IL-1β (1:100) antibodies, followed by HRP-conjugated secondary antibodies and TSA fluorescence labeling (TYR-520Plus for IL-1β). β-actin (1:100) and DAPI were used for cytoskeletal and nuclear counterstaining, respectively. Fluorescence intensity was quantified using ImageJ. Data are presented as mean ± SEM ($n = 3$), with statistical significance assessed by one-way ANOVA ($^*p < 0.05$, $^{**}p < 0.01$).

2.20. Functional enrichment analyses

GO and KEGG enrichment analyses identified overrepresented biological processes, molecular functions, and pathways using hypergeometric tests. GSEA elucidated pathway-level associations of differentially expressed genes. Differential proteins and spatial metabolome profiles were interrogated for cellular roles and biological mechanisms. Protein-protein interaction networks were constructed via STRING. Results were visualized using bar/bubble plots and validated through integrated bioinformatics frameworks.

2.21. Protein-protein interaction network analysis

Protein-protein interaction (PPI) networks were constructed using the STRING database (v11.0) for DEGs. Interactions with a confidence score > 0.8 were retained, and networks were visualized using Cytoscape. Key hub genes and transcription factors were identified based on connectivity and functional annotations.

2.22. Establishment and validation of clinical signatures

Urinary proteomics and targeted metabolomics (LC-MS) identified glycerolipid intermediates and differential proteins in diabetic nephropathy (DN) patients ($n = 20$) versus controls. Diagnostic accuracy was evaluated using ROC analysis, with AUC values quantifying predictive performance. This multi-omics signature was validated via *CNSknowall*, an integrated platform for biomedical data visualization and statistical modeling.

2.23. Statistical analysis

Analyses were conducted in R (v4.1.2) and GraphPad Prism 10. Data are presented as mean ± SEM. Between-group comparisons used two-tailed t-tests (Prism v11.0), with Benjamini-Hochberg-adjusted p-values (significance threshold: $p < 0.05$).

3. Results

3.1. Spatially resolved single-cell atlas of human diabetic nephropathy kidneys

To decode spatial mechanisms underlying DN, we generated a single-cell atlas of human DN kidneys using for FFPE renal puncture biopsies. Histological analysis revealed key pathological features: uniformly distributed glomeruli in the cortex with tubular atrophy and luminal narrowing, significant interstitial fibrosis, and medullary glomerular atrophy with inflammatory infiltrates (Fig. 1a). We annotated two regions-inflammatory and glomerular injury zones-for spatial analysis. Integrating spatial transcriptomics with single-cell RNA sequencing, we constructed a comprehensive atlas of 39,006 high-quality cells from clinical samples (Fig. 1b). Unsupervised clustering (Fig. 1c) identified 10 distinct cell types: red blood cell (6892 cells), interstitial cel (6722 cells), mesenchymal progenitor cell (MPC, 6717 cells)), medullary cell (4761 cells), proximal tubule cell (PTC, 3191 cells)), proliferative cell (2873 cells)), T cell (2658 cells), smooth muscle cell (SMC, 1779 cells), podocyte (1722 cells), and principal cell (1691 cells). Spatial mapping confirmed type-specific distributions (Fig. 1d). Volcano plots prioritized highly expressed genes per cell type (Fig. 1e). Metabolic pathway enrichment of altered clusters (Fig. 1f; Table S3) highlighted podocyte-specific dysregulation in glycerolipid metabolism, MAPK/TNF signaling, tyrosine metabolism, and glutathione metabolism. Strikingly, ROC analysis identified podocytes as the top contributor to DN pathology (AUC = 0.9479; Fig. 1g). Differential expression screening in podocytes yielded 19 key genes (Fig. 1h; Table S4). Protein interaction networks (Fig. 1i) and pathway enrichment (Fig. 1j) confirmed glycerolipid metabolism and MAPK signaling as central hubs, indicating their pivotal role in podocyte dysfunction. This study constructs the spatial single-cell atlas of human DN kidneys, directly linking podocyte-specific dysregulation of glycerolipid-MAPK pathways to metabolic-inflammatory crosstalk.

3.2. Spatial profiling reveals inflammatory cellular landscape and molecular signatures

We deployed spatial transcriptomics to decode the inflammatory microenvironment in human DN kidneys. FFPE tissue sections were analyzed to map histological signatures and pathological cellular landscapes within inflammatory regions (Fig. 2a). Unsupervised clustering identified 10 distinct cell populations in inflammatory zones (Fig. 2b): red blood cell (485 cells), interstitial cell (246 cells), mesenchymal progenitor cell (MPC, 744 cells)), medullary cell (852 cells), proximal tubule cell (PTC, 6 cells)), proliferative cell (295 cells), T cell (610 cells), smooth muscle cell (SMC, 226 cells)), podocyte (205 cells), and principal cell (52 cells) (Fig. 2c). Next, we examined the spatial distribution of the annotated cell types within the human kidney tissue segmentation (Fig. 2d). Spatial mapping confirmed localized enrichment of interstitial cells, proliferative cells, podocyte and principal cells within inflammatory microdomains (Fig. 2e). Differential gene expression analysis revealed 234 histologically significant signatures (195 upregulated; 29 downregulated), including inflammation drivers DUSP4, IL6, and MMP3 (Fig. 2f; Table S5). Pathway enrichment demonstrated convergence on metabolic-inflammatory crosstalk, with insulin resistance, glycerolipid

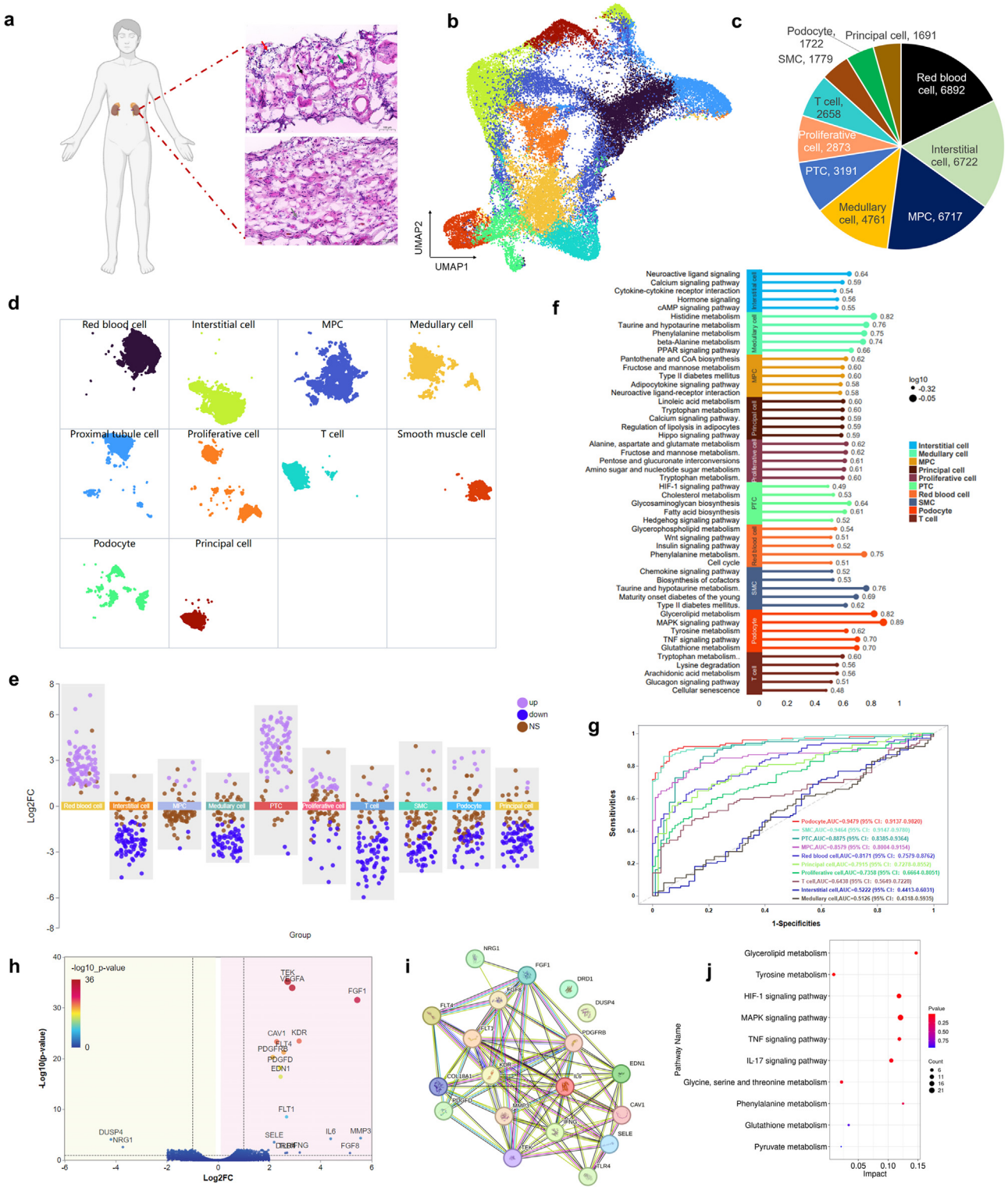

Fig. 1. Spatially resolved cellular atlas of the human kidney reveals histological and molecular architecture. (a) Representative H&E-stained micrograph of human FFPE kidney puncture tissue (scale bar, 100 μm). (b) Visium spatial transcriptomics map annotating major cell types within a kidney section (scale bar, 2 mm). (c) UMAP projection of 10 distinct cell clusters identified by single-cell RNA sequencing (scRNA-seq) method from human FFPE kidney samples ($n = 3$). Cell numbers per cluster are indicated. Clustering performed using Loupe Browser (v8.0). (d) Spatial distribution of annotated cell types across human kidney sections ($n = 3$). (e) Volcano plot identifying differentially expressed genes (DEGs; $|\log_2 FC| > 1$, $p < 0.05$) across annotated cell types. (f) Enriched signaling pathways and associated biological functions for cell type-specific DEGs (GO/KEGG analysis). (g) Receiver operating characteristic (ROC) curves evaluating the diagnostic contribution of key cell types to kidney function. (h) Volcano plot of DEGs in podocytes cell type ($|\log_2 FC| > 1$, $p < 0.05$). (i) Protein-protein interaction network of podocyte DEGs (confidence score > 0.8). (j) Top enriched pathways for podocyte-specific DEGs (GO/KEGG analysis).

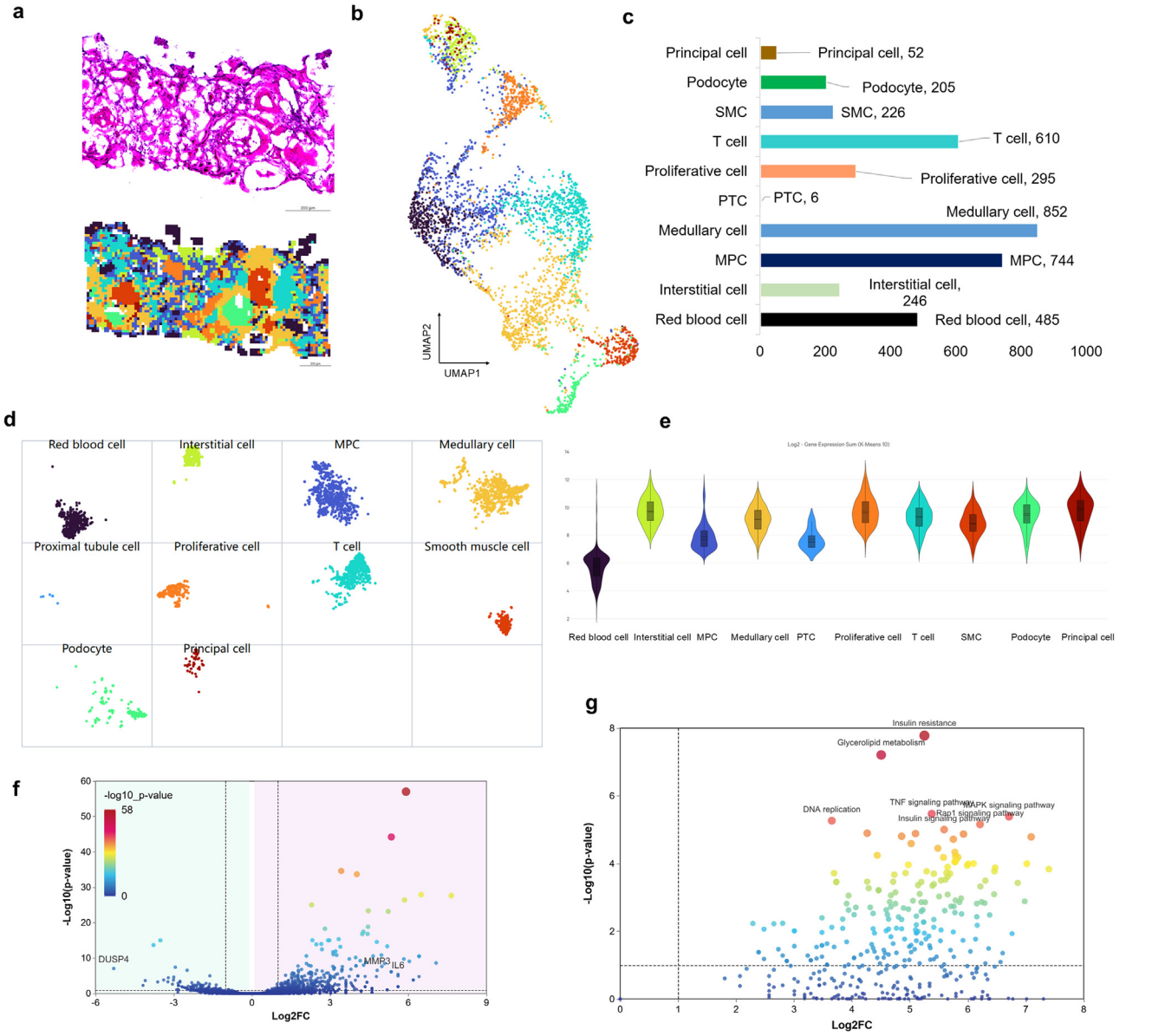

Fig. 2. Inflammatory microregion mapping reveals spatial heterogeneity in diseased human kidney. (a) 10x HD Visium spatial segmentation section of inflammatory microregions in FFPE kidney tissue (top; scale bar, 200 μm) and spatial view of cellular segmentation (bottom; scale bar, 200 μm). (b) Spatial distribution of transcriptionally defined cell clusters within inflammatory microregions. (c) Cell type abundance quantified across inflammatory segmentation of human kidney tissue. (d) Annotated cell type localization within segmented tissue regions. (e) Violin plots showing normalized gene expression per cell cluster. (f) Volcano plot identifying differentially expressed genes (DEGs) in the inflammatory region ($|\log_2 FC| > 1$, $p < 0.05$). (g) Top enriched KEGG pathways from DEGs in inflammatory microdomains.

metabolism, and TNF signaling pathway, as well as MAPK signaling pathway, as top dysregulated processes (Fig. 2g). This spatial atlas uncovers compartmentalized inflammation in DN kidneys, characterized by the inflammatory cellular landscape and molecular signatures as well as metabolic pathway activation.

3.3. Spatial mapping uncovers glomerular injury mechanisms in diabetic nephropathy

We applied spatial transcriptomics to define cellular and molecular signatures within glomerular injury regions of human DN kidneys (Fig. 3a). Spatial profiling revealed distinct cellular colocalization patterns and dominant cell distributions (Fig. 3b). Unsupervised clustering identified 9 key cell populations (Fig. 3c): red blood cell (126 cells), interstitial cell (1859 cells), MPC (1008 cells)), medullary cell (40 cells), PTC (34 cells), proliferative cell (436 cells), T cell (29 cells), podocyte (82 cells), and principal cell (103 cells) (Fig. 3d). Violin plot demonstrated the normalized expression of genes in each cell cluster, and highlighted interstitial cells, PTCs, and principal cells displayed the higher expression levels in the glomerular injury segmentation of human kidney tissue, while notably few podocytes were detected to their relative proportion within the injury zone's cellular composition in our spatial data- indicating region-specific depletion during injury progression (Fig. 3e). Heatmap analysis confirmed cell-type-specific marker expression patterns across these compartments (Fig. 3f). Pathway enrichment demonstrated significant dysregulation of metabolic-inflammatory drivers, with TNF signaling pathway, glycerolipid metabolism, MAPK signaling pathway, and NF-kappa B signaling pathway as top-ranked pathways (Fig. 3g). Differential gene expression analysis identified 179 spatially resolved signatures (Fig. 3h; Table S6), including inflammation

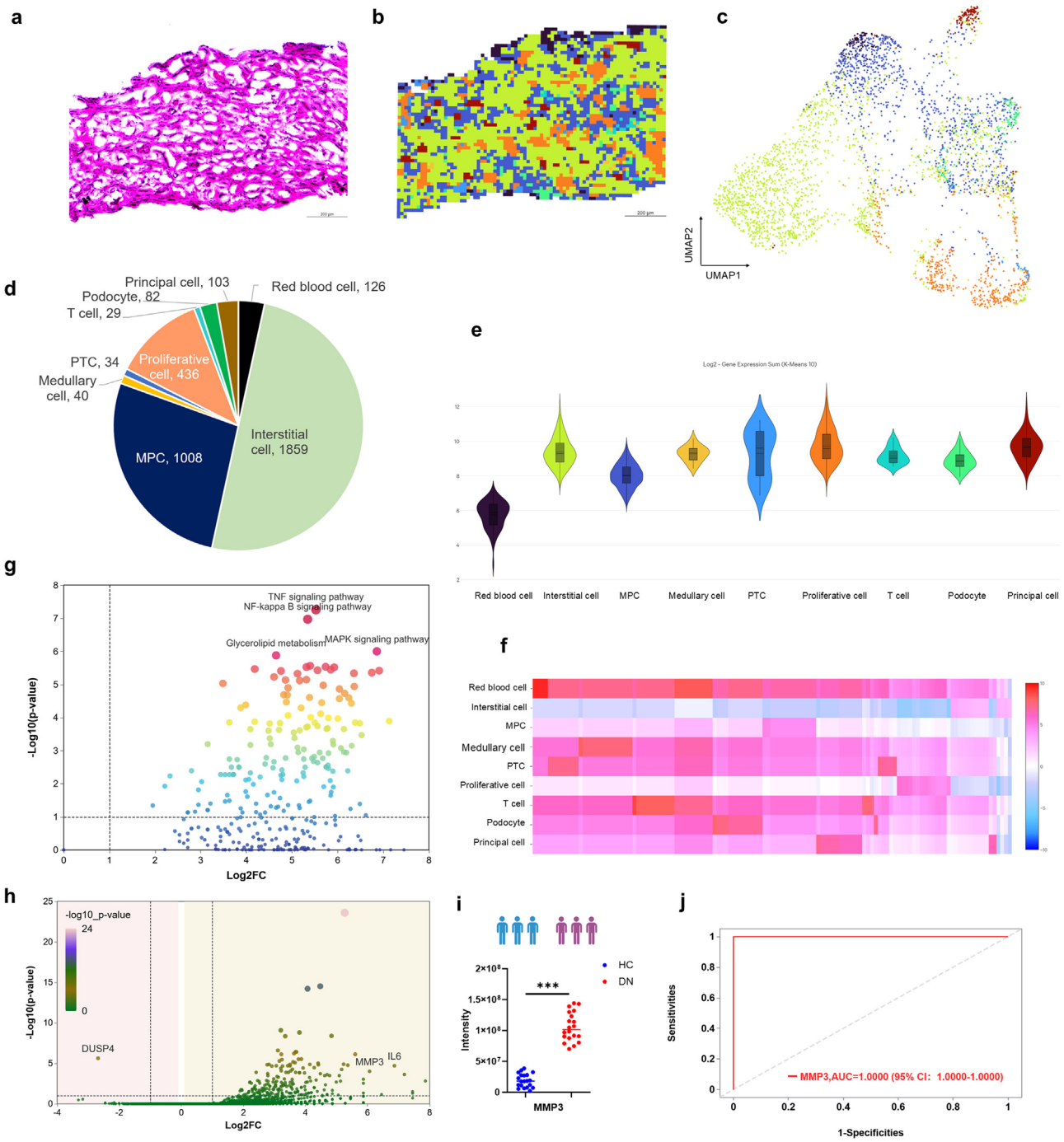

Fig. 3. Spatial transcriptome mapping defined glomerular injury segmentation of human kidney tissue. (a) 10x HD Visium spatial transcriptomics map of human FFPE kidney tissue showing glomerular injury microdomains (scale bar, 200 μm). (b) Spatial distribution of transcriptionally dominant cell states within injured glomeruli (scale bar, 200 μm). (c) UMAP projection identifying 9 distinct cell clusters. (d) Quantitative cell type abundance within glomerular injury regions. (e, Violin plots of normalized gene expression per cell cluster. (f) Heatmap of canonical marker gene expression across cell types (rows: cells; columns: genes). (g) Top enriched KEGG pathways (FDR < 0.05) in glomerular injury regions. (h) Volcano plot of differentially expressed genes (DEGs; $|\log_2 FC| > 1$, $p < 0.05$) in glomerular injury segmentation. (i) Urinary marker protein expression in diabetic nephropathy (DN) patients ($n = 20$) versus healthy controls (HC, $n = 20$; $^{***}p < 0.001$, two-sided t-test). (j) ROC curve validating diagnostic efficacy of markers.

regulators DUSP4, IL6 and MMP3. Critically, urinary MMP3 levels were elevated in DN patients versus controls (Fig. 3i) and exhibited high diagnostic accuracy (AUC = 0.92, Fig. 3j), establishing its potential as a non-invasive biomarker. This integrated spatial atlas reveals how glomerular injury impacts cellular ecosystems through metabolic-inflammatory pathway activation, with MMP3 emerging as both a mechanistic player and clinical indicator.

3.4. Spatial transcriptomics of diabetic mouse kidneys identifies podocyte alterations and MAPK signaling dysregulation

Applying spatial transcriptomics to diabetic (*db/db*) mouse kidneys, we characterized spatial histological alterations and the pathological cellular landscape, mirroring key human DN pathology. Histological analysis demonstrated disrupted cortico-medullary boundaries,

glomerular capillary degeneration, tubular disorganization with luminal narrowing (Fig. 4a, black arrows), and vascular congestion (green arrow). We generated a comprehensive cellular atlas through Visium assays (Fig. 4b), profiling 26,165 high-quality cells (Fig. 4c) and identifying 10 major populations: Loop of Henle cell (5889 cells), NPC (4840 cells), podocyte (3366 cells), epithelial cell (3334 cells), oligodendrocyte (2736 cells), proximal cell (1776 cells), endothelial cell (1532 cells), myeloid cell (1327 cells), pericyte (788 cells), and interstitial cell (577 cells) (Fig. 4d). Spatial mapping confirmed cell-type distributions across pathological regions (Fig. 4e), with comparative expression analysis revealing compartment-specific alterations in diabetic versus control kidneys (Fig. S1a-b). ROC analysis identified podocytes as the most disease-relevant population (Fig. 4f), corroborating our human findings. Spatial reconstruction of podocyte distribution (Fig. 4g) and marker gene localization (Figs. 4h and S2) highlighted their pathological alterations. Critically, we observed the dysregulation of inflammation-metabolism mediators: MMP3 and IL6 were significantly upregulated while DUSP4 was suppressed (Fig. 4i). Pathway enrichment directly implicated MAPK signaling as the central disrupted axis (Fig. 4j), establishing mechanistic continuity with human DN. This cross-species spatial atlas demonstrates that podocyte dysfunction through MAPK pathway dysregulation represents a key driver of DN progression, with MMP3/IL6 induction and DUSP4 suppression serving as fundamental biomarkers.

3.5. Dual-mechanism amelioration of DN via DUSP4-MAPK and glycerolipid metabolic regulation

To definitively confirm our findings and elucidate the spatially resolved impact of ASIV on renal microenvironments in DN, we used an integrated spatial transcriptomics-metabolomics analysis of kidneys from ASIV-treated *db/db* mice. ASIV is a bioactive compound derived from the traditional herb *Astragalus membranaceus* with reported renal protective properties [21,22]. In *db/db* mice, ASIV treatment improved renal histoarchitecture with normalized glomerular distribution despite persistent tubular epithelial irregularities (Fig. 5a). Utilizing 10X Genomics Visium technology, we generated high-resolution spatial maps (Fig. 5b), revealing distinct gene expression patterns across major kidney cell types (Fig. 5c,d), including podocyte-specific signatures (Fig. 5e). Critically, PLS-DA-based VIP score analysis of the spatial transcriptome pinpointed Dusp4, Il6, and Mmp3 as pivotal markers modulated by ASIV (Fig. 5f). Spatial location plots (Fig. 5g) of these canonical marker genes and their co-expression pattern (Fig. 5h) were successfully constructed from spatial transcriptomics dataset. We found that ASIV can significantly reduce expression levels of Il6 and Mmp3, and dramatically increase the level of Dusp4 (Fig. 5i). Concurrent spatial metabolomics uncovered a profound ASIV-mediated reprogramming of glycerolipid metabolism within specific tissue microdomains (Fig. 5j), significantly altering key intermediates including D-glycerate (D-Gly), D-glucose 1-phosphate (G1P), 3-phosphoglycerate (3-PGA), and glycerone phosphate (GNP) (Fig. 5k, Table S7), metabolites classified within the KEGG pathway. Critically, targeted metabolomics of human urine revealed elevated glycerolipid metabolism intermediates in DN patients (n = 20) versus healthy controls (Fig. S3a). D-Gly demonstrated near-perfect diagnostic efficacy (AUC = 0.9975), positioning it as a premier non-invasive biomarker for DN detection (Fig. S3b). Based on these spatial multi-omics insights, Western blot analysis confirmed ASIV's dual-pathway modulation: DUSP4 upregulation directly suppressed MAPK signaling cascades, evidenced by significantly reduced p-p38/p38 and p-JNK/JNK ratios (Fig. 5l). Critically, ASIV concomitantly attenuated pro-inflammatory mediators, significantly lowering MMP3 (Fig. 5m) and IL6 protein expression (Fig. 5n) in diabetic kidneys. This coordinated suppression of IL6/MMP3 not only underscores ASIV's potent anti-inflammatory action but also directly inhibits pathological extracellular matrix degradation, mitigating key drivers of DN progression.

3.6. Podocyte Protection via DUSP4-Mediated Dual Suppression of Inflammatory Signals and Glycerolipid Metabolic Dysfunction

To elucidate ASIV's precise podocyte-protective mechanism against hyperglycemic injury, we employed an integrated multi-omics approach in MPC5 podocytes. Transcriptomic trajectory analysis revealed that ASIV treatment functionally rescued HG-induced perturbations, normalizing cellular states close to untreated controls (Fig. 6a). Volcano plot analysis identified Mmp3, Il6, Il-1β, and Dusp4 as differentially expressed genes, and PLS-DA VIP scoring further confirmed their significant contributions (VIP > 1; Fig. 6c). Notably, we observed that ASIV significantly upregulated Dusp4 while suppressing the inflammatory effectors including Mmp3, IL-1β, and Il6 (Fig. 6d, e). Parallel metabolomics uncovered ASIV-mediated reprogramming of glycerolipid metabolism, specifically reducing key intermediates GNP, 3-PGA, and D-Gly (Fig. 6f). KEGG and GSEA analyses convergently implicated oxidative stress and cytokine/inflammatory pathways as central targets (Fig. 6g,h). Functional validation confirmed ASIV's suppression of ROS and IL-1β via immunofluorescence quantification (Fig. 6i), mechanistically linking transcriptomic-metabolomic signatures to podocyte protection. This work provides the first demonstration that ASIV orchestrates podocyte salvage through a dual DUSP4-centric mechanism: Direct transcriptional repression of Mmp3/Il6/Il1b to quench inflammation and matrix degradation; and Metabolic recalibration via glycerolipid pathway modulation, thereby neutralizing oxidative stress. The coordinated DUSP4-mediated suppression of both inflammatory signaling and glycerolipid derangement represents a novel therapeutic axis against diabetic podocytopathy.

4. Discussion

We developed a spatial multi-omics platform to deconstruct DN microenvironments using clinically relevant FFPE biopsies, overcoming critical limitations in spatial genomics. Our high-resolution mapping of 39,006 cells across cortical and medullary regions identified 10 distinct cell populations and their spatial relationships in DN progression. This unprecedented atlas reveals not only cellular composition but crucially their spatial organization and niche-specific contributions to disease pathogenesis [23–26]. Most significantly, we demonstrate that podocyte injury serves as a principal driver of DN pathology through compartment-specific dysregulation of the glycerolipid metabolism-MAPK signaling axis. Integration of spatial transcriptomics with metabolomics further identified ASIV as a novel dual-pathway modulator targeting this network, providing new therapeutic opportunities for precision intervention in DN.

Our spatial mapping reveals podocytes as active metabolic-inflammatory hubs, not passive injury targets as traditionally viewed [27]. Surviving podocytes in injury zones undergo profound metabolic rewiring, accumulating intermediates that activate MAPK cascades. This podocyte-centric axis likely interacts with spatially coordinated immune responses. Recent spatial multi-omics studies have delineated macrophage-dominated inflammatory niches in DN, where M1 polarization and suppressed Arg1-mediated arginine metabolism create a pro-inflammatory, dysfunctional metabolism microenvironment [12]. Spatial co-localization analyses show these dysregulated podocytes directly interface with MMP3/IL6-enriched zones, where podocyte-derived signals recruit inflammatory infiltrates that exacerbate matrix degradation. This mechanism is conserved in diabetic mice, where podocyte-specific MAPK dysregulation correlates with cortico-medullary disruption. The spatial metabolomics-transcriptomics integration demonstrates how lipid accumulation impairs podocyte function while simultaneously activating inflammatory pathways through DUSP4 suppression. This vicious cycle of metabolic stress and inflammation within glomerular niches represents a fundamental mechanistic advance, positioning podocyte dysfunction as an earlier trigger for fibrotic microenvironment amplification than previously recognized tubular events [28].

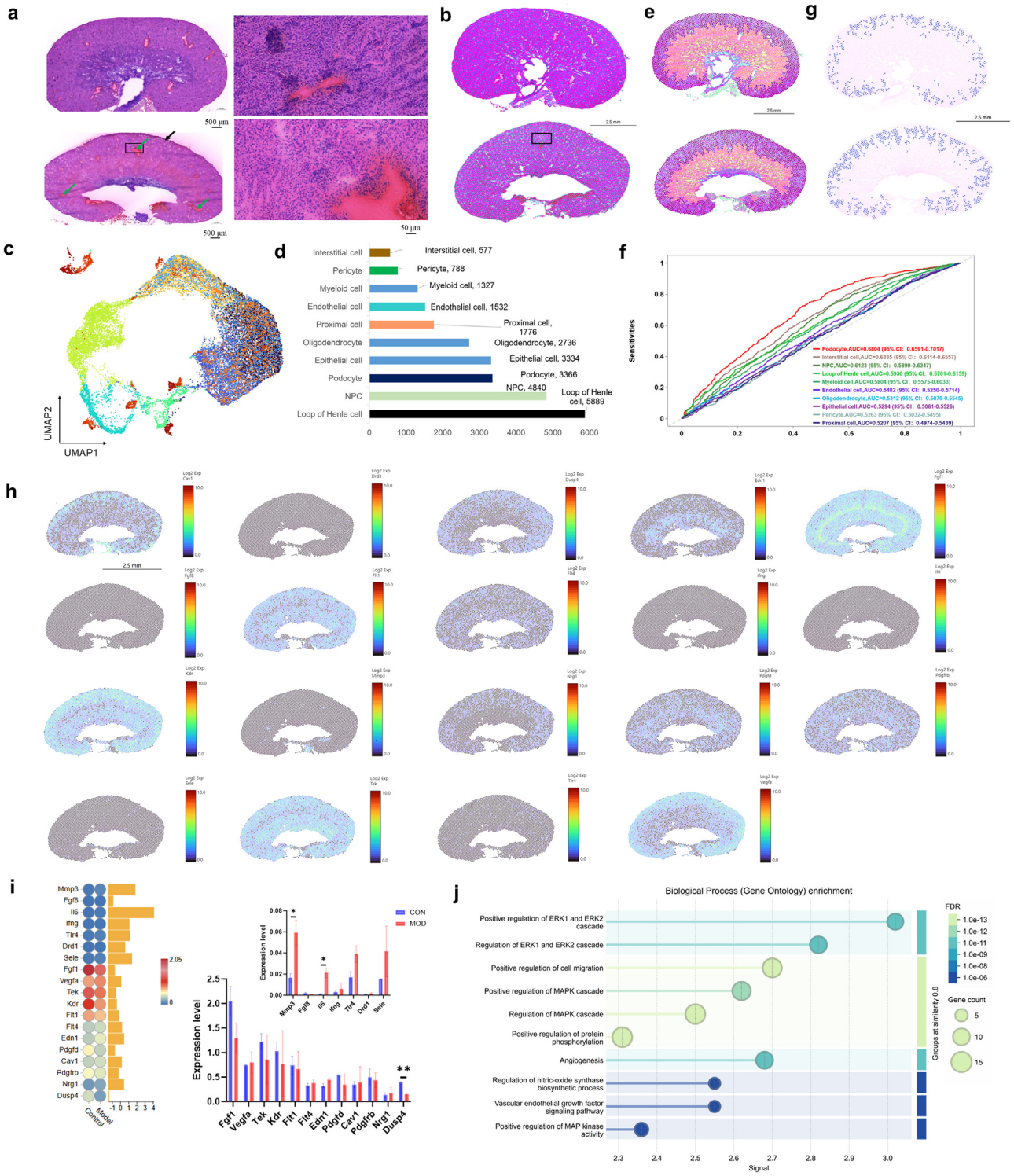

Fig. 4. Spatially resolved atlas of diabetic mice kidney reveals cell-specific transcriptional signatures. (a) H&E-stained kidney sections: Control vs. diabetic (*db/db*) mice (scale bars, 500 μm) with zoomed pathological features (scale bars, 50 μm). (b) Single-cell RNA-seq (scRNA-seq) maps of control (top) and *db/db* (bottom) kidneys (scale bars, 2.5 μm). (c) UMAP projection of 26,165 cells from diabetic kidney transcriptomes. (d) Quantified abundance of annotated cell types. (e) Visium spatial mapping of cell types in control (top) and *db/db* (bottom) kidneys (scale bars, 2.5 μm). (f) ROC curves evaluating diagnostic contribution of key cell types to diabetic pathology. (g) Podocyte spatial distribution in diabetic glomeruli (Visium). (h) Spatial localization of canonical marker genes in *db/db* kidneys (10x Visium CytAssist; scale bar, 2.5 μm). (i) Differential expression of marker genes in control vs. *db/db* mice (mean ± SD; $^{*}p < 0.05$, $^{**}p < 0.01$, two-sided t-test). (j) Gene ontology enrichment pathway of canonical marker genes.

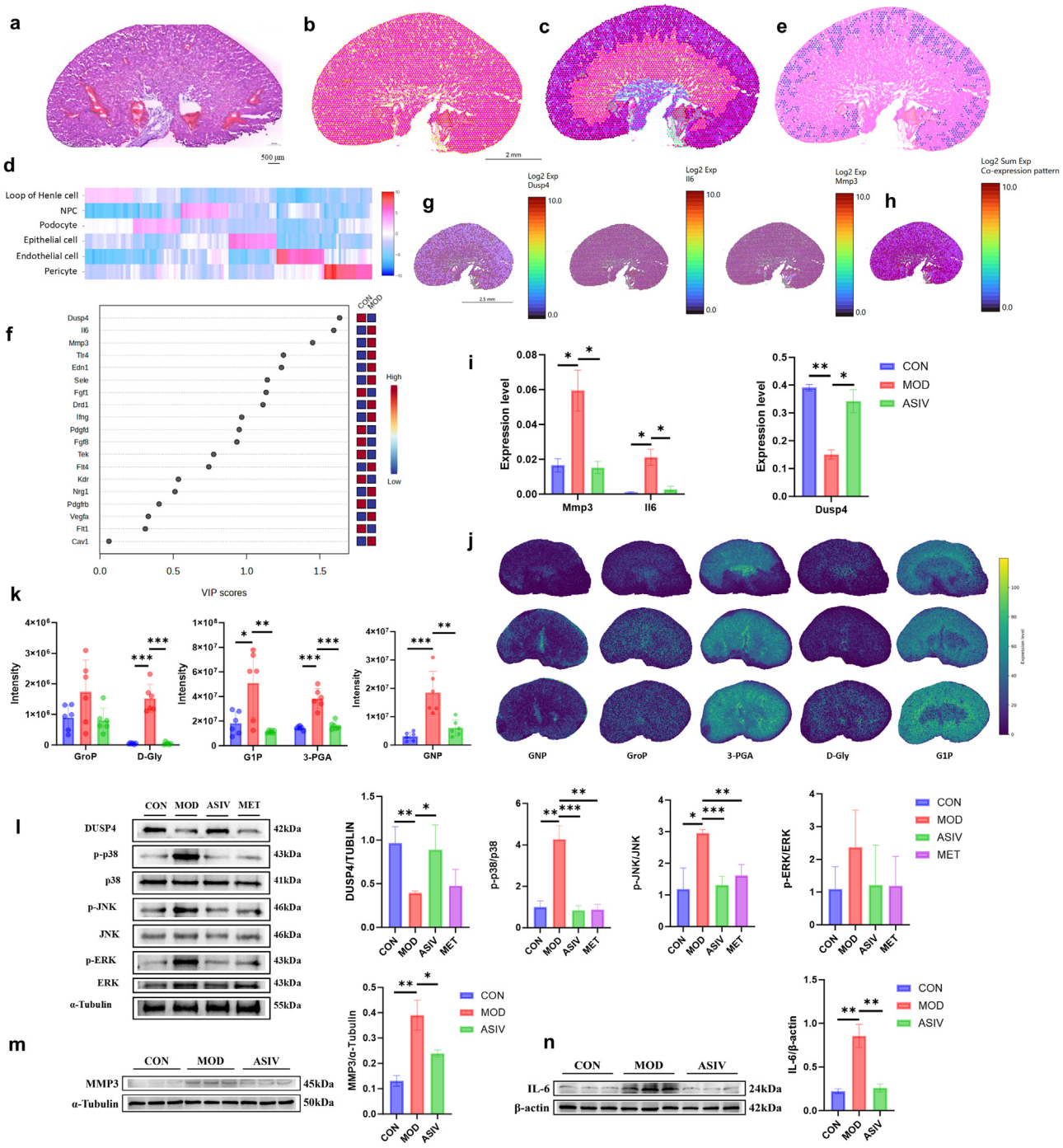

Fig. 5. Spatial transcriptomics and metabolomics reveal ASIV regulating diabetic kidney microenvironments. (a) H&E-stained kidney section from ASIV-treated *db/db* mouse (scale bar, 500 μm). (b) Visium spatial feature spots in ASIV-treated diabetic kidney (scale bar, 2 mm). (c) Spatial transcriptomic atlas of ASIV-treated *db/db* kidney (scale bar, 2 mm). (d) Heatmap of cell cluster-specific genes from scRNA-seq (rows: cells; columns: genes). (e) Podocyte spatial redistribution following ASIV treatment. (f) PLS-DA VIP scores identifying therapeutic response markers. (g) Spatial mapping of therapeutic response genes *Dusp4, Il6*, and *Mmp3* (scale bar, 2.5 μm). (h) Co-expression pattern of Dusp4-Il6-Mmp3 across tissue domains. (i) Differential expression of *Dusp4, Il6*, and *Mmp3* (Control vs. *db/db* vs. ASIV; mean ± SD; $^{*}p < 0.05$, $^{**}p < 0.01$, $^{***}p < 0.001$, $n = 3$). (j) MALDI imaging of glycerolipid metabolism intermediates: Glycerophosphoric acid (GroP), D-glucose 1-phosphate (G1P), glycerone phosphate (GNP), 3-phosphoglycerate (3-PGA), and D-glycerate (D-Gly) (scale bars, 200 μm; $^{*}p < 0.05$, $^{**}p < 0.01$). (k) Quantified metabolites of glycerolipid metabolism across groups (mean ± SD; $^{***}p < 0.001$ vs. *db/db*). (l) Western blot of MAPK pathway proteins (*Dusp4*/p-ERK/t-ERK shown; $^{*}p < 0.05$ vs. *db/db, n* = 3). (m) MMP3 protein expression validation (mean ± SD; $^{**}p < 0.01$ vs. *db/db, n* = 3). (n) IL-6 suppression by ASIV (mean ± SD; $^{**}p < 0.01$ vs. *db/db, n* = 3).

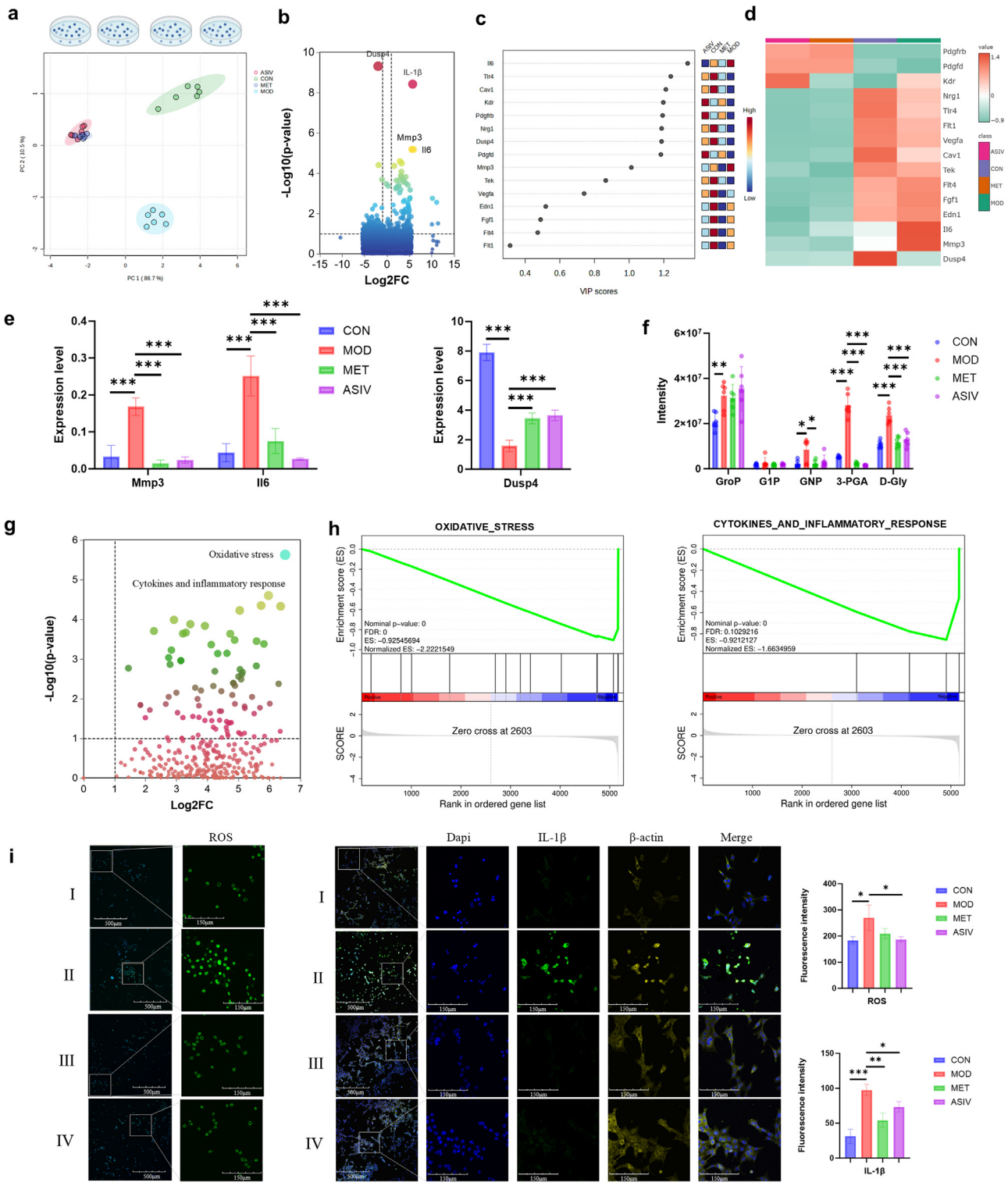

Fig. 6. ASIV protects podocytes from high glucose-induced injury via multi-omics regulation of metabolic and inflammatory pathways. (a) PCA of MPC5 podocyte transcriptomes after 24 h treatments (Control, High Glucose [HG, model group], HG + ASIV, HG + MET). (b) Volcano plot of HG-induced DEGs (*Mmp3, IL-1β, Il6, Dusp4*; $|\log_2 FC| > 2$, $p < 0.05$). (c) PLS-DA VIP ranking of therapeutic response markers. (d) Heatmap of targeted DEGs across conditions (z-score scaled; rows: genes; columns: samples). (e) Expression of *Dusp4, Il6*, and *Mmp3* ($^{*}p < 0.001$ vs. HG; $n = 6$). (f) Glycerolipid metabolism intermediates: GroP, G1P, GNP, 3-PGA, D-Gly ($^{*}p < 0.001$, $^{**}p < 0.01$ vs. HG; $n = 6$). (g) Top enriched KEGG pathways (oxidative stress, cytokines and inflammatory response). (h) GSEA confirming pathway enrichment (FDR < 0.25). (i) Immunofluorescence quantification: ASIV reduces ROS and IL-1β in HG-stressed podocytes (scale bars: 150 μm; $^{*}p < 0.05$, $^{**}p < 0.01$, $^{***}p < 0.001$ vs. HG; $n = 3$).

Cross-species spatial analysis of human DN and *db/db* mouse kidneys revealed conserved pathogenic pathways in glomerular injury zones, including TNF signaling, glycerolipid metabolism, and NF-κB signaling. Podocytes emerged as major contributors across species [29,30], validating their central role. Spatial mapping specifically identified MMP3 upregulation within the human glomerular injury microregion, leading to its validation as a urinary biomarker. Clinical analyses demonstrated elevated urinary MMP3 levels with high diagnostic accuracy, directly linking biomarker detection to active injury sites. This spatial origin specificity provides a strong biological rationale for MMP3 as a non-invasive monitoring tool, representing a significant advance in DN clinical treatment.

In this study, we selected astragaloside IV (ASIV), a primary bioactive saponin derived from the traditional medicinal herb *Astragalus membranaceus*, for mechanistic exploration based on its established pharmacological profile and potential relevance to DN pathogenesis. ASIV has been widely documented for its renoprotective effects in experimental diabetes, including anti-fibrotic, anti-inflammatory, and antioxidant activities [21,22]. Notably, prior evidence suggests that ASIV can modulate metabolic pathways and mitigate glomerular injury, yet its spatially-specific mechanism within human diabetic kidneys remains uncharted. Given our spatial atlas identifying podocyte-centered glycerolipid-MAPK dysregulation as a core pathogenic axis, we hypothesized that ASIV-with its reported multi-target capabilities-might simultaneously correct metabolic reprogramming and suppress inflammatory signaling. This opinion led us to investigate ASIV as a promising candidate to disrupt the spatially organized metabolic-inflammatory crosstalk in DN, offering a tangible therapeutic translation of our atlas-driven discovery.

We then demonstrated ASIV's remarkable therapeutic potential through dual-pathway modulation: DUSP4-mediated MAPK suppression and glycerolipid metabolic normalization. Notably, the therapeutic effects of ASIV extends to immune modulation within the renal microenvironment. Complementary spatial study showed that ASIV can simultaneously target macrophage-dominated inflammatory niches by restoring Arg1 expression and reprogramming arginine metabolism, thereby mitigating another key dimension of DN pathogenesis [22]. This multi-target, multi-cellular action underscores ASIV's polypharmacology, which specifically targets the integrated metabolism-inflammation axis in DN. In this study, spatial multi-omics in ASIV-treated mice showed specific upregulation of Dusp4 with parallel reductions in Il6 and Mmp3. Mechanistic studies revealed ASIV acts as a master regulator, simultaneously addressing oxidative stress on glycerolipid control and inflammation via MAPK inhibition. In vitro validation using injured podocytes confirmed protection through: inflammatory mediator downregulation (Mmp3, Il6, IL-1β), Dusp4 restoration, and metabolic normalization. The ASIV's polypharmacology specifically targets DN's metabolism-inflammation, with DUSP4 upregulation serving as a critical switch suppressing p38/JNK phosphorylation and downstream effectors.

Our study redefines DN pathogenesis through three transformative advances: A spatial single-cell atlas enabling direct human microenvironment analysis, MMP3 as a spatially validated diagnostic biomarker, and ASIV's dual-pathway therapeutic mechanism. By establishing podocytes as spatially organized metabolic-inflammatory hubs driving disease through a conserved glycerolipid-MAPK axis, we shift the DN paradigm from glomerulocentric to niche-specific understanding. While our data demonstrate a strong correlative rescue of both metabolic and inflammatory phenotypes by ASIV, we acknowledge that this joint regulation cannot establish a clear causal relationship yet, from our data. Future studies employing genetic perturbation of DUSP4 or key metabolic enzymes are needed to dissect the precise hierarchical relationship within this integrated axis. Future work should focus on: longitudinal spatial mapping of disease progression, upstream triggers of podocyte metabolic reprogramming, cell-cell communication networks, and large-scale MMP3 clinical validation. This study also has limitations regarding orthogonal validation due to the scarcity of clinical biopsy material, which precluded extensive immunofluorescence or ELISA assays. This work exemplifies how spatial multi-omics can bridge molecular mechanisms and clinical translation, offering both diagnostic and therapeutic advances for DN while providing a framework for investigating microdomain-specific drivers in other chronic diseases.

5. Conclusion

In this study, we generated the spatially resolved single-cell atlas of human DN kidneys using clinical FFPE biopsies, integrating transcriptomics, metabolomics, and histopathology to dissect compartment-specific pathogenesis. Our atlas reveals podocytes as metabolic-inflammatory hubs within glomerular injury zones, where glycerolipid accumulation promotes MAPK hyperactivation via DUSP4 suppression, driving IL-6/MMP3-mediated matrix degradation. Cross-species spatial profiling in diabetic mice confirmed podocyte-specific MAPK dysregulation as a conserved disease driver. Critically, we identified urinary MMP3-directly mapped to injured human glomeruli-as a non-invasive biomarker. We further demonstrate that ASIV disrupts this cycle via dual-pathway targeting: DUSP4-mediated MAPK inhibition and glycerolipid metabolic reprogramming to rescue podocyte integrity. This work redefines DN as a disorder of spatially organized metabolic-inflammation synergy and establishes a biomarker-guided therapeutic framework.

CRediT authorship contribution statement

Shi Qiu: Writing – review & editing, Writing – original draft, Methodology, Investigation, Funding acquisition, Conceptualization. **Zhibo Wang:** Methodology, Investigation, Data curation. **Sifan Guo:** Methodology, Investigation, Data curation. **Dandan Xie:** Methodology, Investigation. **Ying Cai:** Methodology, Investigation. **Xian Wang:** Methodology, Investigation. **Qiang Yang:** Methodology, Investigation. **Qiqi Zhao:** Methodology, Investigation. **Yu Guan:** Methodology, Investigation. **Chunsheng Lin:** Methodology, Investigation. **Hong Yao:** Methodology, Investigation. **Songqi Tang:** Supervision, Resources, Methodology, Investigation, Conceptualization. **Wenjie Sun:** Supervision, Resources, Methodology, Investigation, Conceptualization. **Yiqiang Xie:** Writing – review & editing, Writing – original draft, Supervision, Resources, Methodology, Investigation, Funding acquisition, Data curation, Conceptualization. **Aihua Zhang:** Writing – review & editing, Writing – original draft, Visualization, Validation, Supervision, Software, Resources, Project administration, Methodology, Investigation, Funding acquisition, Formal analysis, Data curation, Conceptualization.

Declaration of competing interest

The authors declare that they have no conflicts of interest in this work.

Acknowledgments

The authors are grateful for the generous support from the Program of the National Natural Science Foundation of China (81973745, 82104733, and 82560836), Natural Science Foundation of Heilongjiang Province (YQ2019H030), Hainan Province Nanhai New Star Science and Technology Innovation Talent Platform Project by Hainan Provincial Department of Science and Technology (NHXXRCXM202317), Academic Enhancement Support Program by Hainan Medical University (XSTS2025079), Talent Lift Engineering Project of China Association of TCM (QNRC2-B06). The authors wish to thank Shanghai OE Biotech for their technical assistance.

Supplementary materials

Supplementary material associated with this article can be found, in the online version, at doi:10.1016/j.fmre.2026.02.005.

References

[1] F. Karimi, M. Moazamfard, R. Taghvaeefar, et al., Early detection of diabetic nephropathy based on urinary and serum biomarkers: An updated systematic review, Adv. Biomed. Res. 13 (2024) 104.

[2] D. Xie, Y. Zhu, S. Guo, et al., The metformin mediated MAPK signaling pathway influences D-Xylose regulation during diabetic kidney disease therapy, Commun. Med. (Lond.) 5 (1) (2025) 454.

[3] C. Kuppe, M.M. Ibrahim, J. Kranz, et al., Decoding myofibroblast origins in human kidney fibrosis, Nature 589 (7841) (2021) 281–286.

[4] A. Larnane, C. Lefèvre-Horgues, C. Cruaud, et al., Characterization of challenging forensic DNA traces using advanced molecular technologies, Int. J. Legal Med. 139 (4) (2025) 1511–1527.

[5] S. Qiu, Y. Cai, H. Yao, et al., Small molecule metabolites: Discovery of biomarkers and therapeutic targets, Signal Transduct. Target. Ther. 8 (1) (2023) 132.

[6] Y. Cai, Z. Wang, S. Guo, et al., Detection, mechanisms, and therapeutic implications of oncometabolites, Trends Endocrinol. Metab. 34 (12) (2023) 849–861.

[7] B.B. Lake, S. Chen, M. Hoshi, et al., A single-nucleus RNA-sequencing pipeline to decipher the molecular anatomy and pathophysiology of human kidneys, Nat. Commun. 10 (1) (2019) 2832.

[8] B.J. Stewart, J.R. Ferdinand, M.D. Young, et al., Spatiotemporal immune zonation of the human kidney, Science 365 (6460) (2019) 1461–1466.

[9] S. Qiu, Z. Wang, S. Guo, et al., Single cell sequencing and spatial multiomics of diabetic kidney segmentation insights zonation-specific therapeutic metabolic pathways, Cell Insight 4 (3) (2025) 100252.

[10] A. Faivre, M. Bugarski, A. Rinaldi, et al., Spatiotemporal landscape of kidney tubular responses to glomerular proteinuria, J. Am. Soc. Nephrol. 35 (7) (2024) 854–869.

[11] Y. Muto, P.C. Wilson, N. Ledru, et al., Single cell transcriptional and chromatin accessibility profiling redefine cellular heterogeneity in the adult human kidney, Nat. Commun. 12 (1) (2021) 2190.

[12] S. Qiu, Z. Wang, S. Guo, et al., Spatial transcriptomics and metabolomics reveal astragaloside IV as a microenvironment-targeted regulator of arginine metabolism in inflammatory microregions of diabetic kidney, J. Future Foods (2026), doi:10.1016/j.jfutfo.2026.01.017.

[13] S. Qiu, Z. Wang, X. Wang, et al., Spatial metabolomics identifies riboflavin metabolism as a therapeutic target of Huangqi Guizhi Wuwu decoction in diabetic nephropathy, Biomed. Chromatogr. 39 (11) (2025) e70239.

[14] Y. Xie, D. Xie, S. Guo, et al., Spatial metabolic and protein profiles reveal astragaloside IV attenuates diabetic nephropathy by inhibiting ST13 acetylation at lysine 14 to restore amino acid metabolism dysregulation, J. Future Foods (2025), doi:10.1016/j.jfutfo.2025.10.017.

[15] T. Doke, A. Abedini, D.L. Aldridge, et al., Single-cell analysis identifies the interaction of altered proximal tubules with the immune and metabolic microenvironment in early diabetic kidney disease, Kidney Int. 101 (4) (2022) 748–764.

[16] P.C. Wilson, H. Wu, Y. Kirita, et al., The single-cell transcriptomic landscape of early human diabetic nephropathy, Proc. Natl. Acad. Sci. U S A 116 (39) (2019) 19619–19625.

[17] S. Qiu, S. Guo, D. Xie, et al., Comprehensive multiomics revealed astragaloside IV regulating carbohydrate metabolism dysfunction through clinical, animal and cellular platforms, Food Biosci. 68 (2025) 106757.

[18] S. Qiu, S. Guo, Z. Wang, et al., Integrated metabolomics and proteomics revealed astragaloside IV inhibiting Pdxk-mediated vitamin B6 metabolism based on liquid chromatography-tandem mass spectrometry combined with pattern recognition and correlation analysis, J. Funct. Foods 124 (2025) 106654.

[19] X. Chen, S. Guo, D. Xie, et al., Mass spectrometry-based Multi-omics profiling identifies bioactive compound astragaloside IV as a therapeutic agent targeting Cltc K856 acetylation to restore tyrosine metabolic zonation in diabetic nephropathy, J. Future Foods (2025), doi:10.1016/j.jfutfo.2025.09.020.

[20] S. Qiu, D. Xie, S. Guo, et al., Spatially segregated multiomics decodes metformin-mediated functional-specific metabolic characteristics in diabetic kidney disease, Life Metab. 4 (5) (2025) loaf019.

[21] S. Qiu, S. Guo, D. Xie, et al., Metabolite-guided acetylation therapy: Astragaloside IV reverses diabetic nephropathy via Gna13-driven purine metabolic reprogramming, Food Front. 6 (2025) 2961–2974.

[22] S. Qiu, S. Guo, D. Xie, et al., Spatial multi-omics dissection of astragaloside IV in diabetic kidney zonation: a food-derived bioactive regulator of metabolic and proteomic landscapes, J. Future Foods (2025), doi:10.1016/j.jfutfo.2025.07.027.

[23] X. Meng, W. Li, J. Xu, et al., Spatiotemporal transcriptome atlas of developing mouse lung, Sci. Bull. (Beijing) 70 (10) (2025) 1641–1658.

[24] Q. Yang, Y. Cai, Y. Guan, et al., Metabolic phenotypes: Molecular bridges between health homeostasis and disease imbalance, Comput. Struct. Biotechnol. J. 27 (2025) 4710–4719.

[25] L. Chen, J.Z. Clark, J.W. Nelson, et al., Renal-tubule epithelial cell nomenclature for single-cell RNA-sequencing studies, J. Am. Soc. Nephrol. 30 (8) (2019) 1358–1364.

[26] Q. Yang, Y. Cai, S. Guo, et al., Localization analysis of metabolites from complex biological samples-recent analytical technique of mass spectrometry imaging, Front. Mol. Biosci. 10 (2023) 1169449.

[27] J. Park, R. Shrestha, C. Qiu, et al., Single-cell transcriptomics of the mouse kidney reveals potential cellular targets of kidney disease, Science 360 (6390) (2018) 758–763.

[28] K. Umanath, J.B. Lewis, Update on Diabetic nephropathy: Core curriculum 2018, Am. J. Kidney Dis. 71 (6) (2018) 884–895.

[29] J. Yang, Z. Zheng, Y. Jiao, et al., Spotiphy enables single-cell spatial whole transcriptomics across an entire section, Nat. Methods 22 (4) (2025) 724–736.

[30] B.B. Lake, R. Menon, S. Winfree, et al., An atlas of healthy and injured cell states and niches in the human kidney, Nature 619 (7970) (2023) 585–594.

Author profile

Shi Qiu is a distinguished researcher recognized as a Class D Talent in the Hainan Free Trade Port and Hainan Medical University, China. Her research focuses on pharmaceutical analysis, and metabolomics. She presides over the Youth Project and Regional Project of National Natural Science Foundation of China, and Nanhai New Star Project. She has authored over 40 SCI-indexed papers in reputable journals, and holds 10 national software copyrights as the first inventor. Her work has obtained over 2340 citations, achieving an H-index of 24.

Aihua Zhang is a doctoral supervisor and principal investigator at Hainan Medical University, China. He holds prestigious fellowships including Member of the European Academy of Sciences and Arts (Austria) and Fellow of the Royal Society of Chemistry (UK). His research focuses on pharmacological sciences, therapeutic targets, and metabolomics. He has published over 350 papers (H-index: 72, > 16,900 citations), and holds 60 patents. He is recognized among the world's top scientists (Highly Ranked Scholars-Lifetime, Stanford's top 2%, Best Medicine Scientists in China) and has received numerous awards, including the IAAM Scientist Medal (Sweden) and SERVIER Investigator Award in Pharmacology (France).